

RESEARCH ARTICLE SUMMARY

NEUROSCIENCE

Three-dimensional Ca²⁺ imaging advances understanding of astrocyte biology

Erika Bindocci,* Iaroslav Savtchouk,* Nicolas Liaudet,* Denise Becker, Giovanni Carriero, Andrea Volterra†

INTRODUCTION: Astrocytes translate incoming information and generate functional outputs via Ca²⁺ signaling. Thereby, they respond to neuronal activity, producing downstream modulation of synaptic functions, and may participate in hemodynamics regulation. Deciphering the “Ca²⁺ language” of astrocytes is therefore essential for defining their roles in brain physiology and pathology. However, the specifics of astrocytic Ca²⁺ signaling are still poorly understood, and recent studies producing inconsistent or contradictory results have fostered debate on the actual role of astrocytes in synaptic and vascular functions.

RATIONALE: A neglected potential source of inconsistencies lies in the way astrocytic Ca²⁺ signaling has been studied to date, mostly by conventional two-dimensional (2D) imaging,

which assumes that sampling a single (~1 μm) focal plane is representative of the entire astrocytic cell. This is, however, dubious given that astrocytes are highly 3D cells, entertain heterogeneous 3D relations with neighboring structures, and display Ca²⁺ signals on a local scale. Therefore, we developed a new method to three-dimensionally scan entire astrocytes and observe full-cell Ca²⁺ dynamics.

RESULTS: With our 3D approach, we sampled astrocytes at a sufficient rate to detect events with durations of >1.5 s throughout the cell, and faster ones in selected substructures. We found that Ca²⁺ activity in an individual astrocyte is heterogeneously scattered throughout the cell, largely compartmented within each region, and preponderantly local. The majority resides in the “gliapil,”

the peripheral region composed of fine (optically subresolved) structures occupying ~75% of the astrocyte volume. Within the central (resolvable) “core,” the soma is mostly inactive, whereas processes are frequently active yet show widely different activity between them. Even in individual processes, activity distributes heterogeneously, with alternating “hot” and “cold” spots.

We performed 3D imaging in awake mice and in adult brain slices. Activity *in vivo* was faster

ON OUR WEBSITE

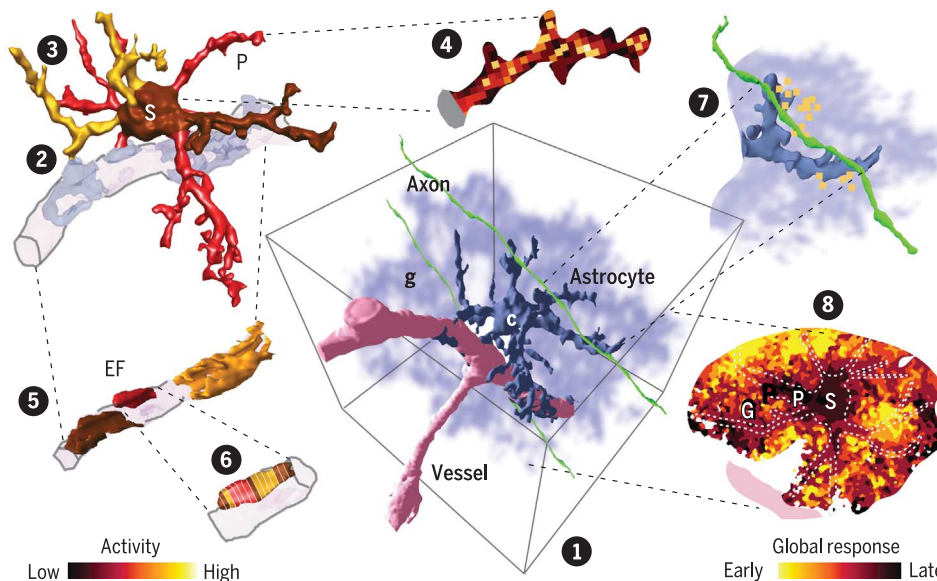
Read the full article at <http://dx.doi.org/10.1126/science.aai8185>

and more frequent, particularly in endfeet, yet similar in properties and cellular distribution to slices, except for the presence of cell-wide “global” Ca²⁺ events mainly associated with

mouse movement. Contrary to current beliefs, global events were not sweeping waves, but rather consisted of multifocal Ca²⁺ elevations that started at multiple gliapil loci and then spread to the core.

At the vascular interface, astrocytic Ca²⁺ activity was mostly restricted to individual endfeet, even to their fractions, and only occasionally coordinated with the endfoot process or the rest of the astrocyte. Two or more endfeet were mainly asynchronous, even when enwrapping the same vessel. Astrocytic structures and axons intersected three-dimensionally, and minimal axonal activity (individual action potentials) produced time-correlated astrocytic Ca²⁺ elevations in small spots (<1% of the volume), which demonstrates that astrocytes can sense even the lowest levels of neuronal activity.

CONCLUSION: We provide the first comprehensive 3D map of Ca²⁺ activity in an individual astrocyte. Its widespread, heterogeneous, local, and mostly 3D nature confirms the appropriateness of our whole-cell imaging approach. Past 2D studies, often focusing on somatic Ca²⁺ dynamics, inadequately described the emerging richness and complexity of the astrocyte activity, notably at astrocyte-synapse and astrocyte-vascular interfaces, where activity is small, fast, and frequent. In this context, we can foresee future challenges in extending studies to the gliapil, whose structures fall below current optical resolution, and in reporting the complete gamut of astrocyte Ca²⁺ signals at the whole-cell scale, both requiring technical advances. Nonetheless, the technique demonstrated here promises to make 3D Ca²⁺ imaging the state-of-the-art approach for Ca²⁺ studies addressing the role of astrocytes in brain function. ■



3D Ca²⁺ imaging reveals the complex activity of astrocytes. (1) Representation of the 3D structural interactions among astrocyte, axons, and blood vessels. The astrocyte contains optically resolved (c, core) and unresolved (g, gliapil) regions. (2) 3D Ca²⁺ imaging reveals different activity (intensity color scale) in different astrocytic regions (P, processes; S, soma; EF, endfoot); (3) in different processes; and (4) in different loci of individual processes. (5) It also reveals asynchronous activity in endfeet, (6) often restricted to endfoot subdomains, and (7) local astrocyte responses to minimal axonal firing, or (8) global responses to *in vivo* locomotion (time color scale).

Department of Fundamental Neuroscience, University of Lausanne, 1005 Lausanne, Switzerland.

*These authors contributed equally to this work.
†Corresponding author. Email: andrea.volterra@unil.ch
Cite this article as E. Bindocci *et al.*, *Science* 356, eaa8185 (2017). DOI: 10.1126/science.aai8185

RESEARCH ARTICLE

NEUROSCIENCE

Three-dimensional Ca²⁺ imaging advances understanding of astrocyte biology

Erika Bindocci,* Iaroslav Savtchouk,* Nicolas Liaudet,* Denise Becker, Giovanni Carriero, Andrea Volterra†

Astrocyte communication is typically studied by two-dimensional calcium ion (Ca²⁺) imaging, but this method has not yielded conclusive data on the role of astrocytes in synaptic and vascular function. We developed a three-dimensional two-photon imaging approach and studied Ca²⁺ dynamics in entire astrocyte volumes, including during axon-astrocyte interactions. In both awake mice and brain slices, we found that Ca²⁺ activity in an individual astrocyte is scattered throughout the cell, largely compartmented between regions, preponderantly local within regions, and heterogeneously distributed regionally and locally. Processes and endfeet displayed frequent fast activity, whereas the soma was infrequently active. In awake mice, activity was higher than in brain slices, particularly in endfeet and processes, and displayed occasional multifocal cellwide events. Astrocytes responded locally to minimal axonal firing with time-correlated Ca²⁺ spots.

Astrocytes translate information received from neighboring central nervous system cells and generate modulatory responses at the local or network level via Ca²⁺ signaling (1–6). In response to neuronal activity, they show intracellular Ca²⁺ elevations (7–10) that result in downstream effects on synaptic transmission and plasticity (11–15). Astrocytic Ca²⁺ elevations also trigger vascular responses that may be involved in the control of cerebral blood flow (16–19). Therefore, deciphering the “Ca²⁺ language” of astrocytes is an essential step toward defining their role in physiological and pathophysiological brain function. However, the modalities and implications of astrocytic Ca²⁺ signaling are still not well understood. In each domain in which some studies have identified a specific role for this signaling (7, 11–15, 20, 21), other studies reported inconsistent results (22–26), casting doubt on the original observations and fostering controversy.

A neglected aspect in astrocyte studies and a potential source of inconsistency is the spatial limitation imposed by two-photon Ca²⁺ imaging. Even the most technically advanced studies so far have monitored only small portions of total astrocytes, contained in a single one-dimensional (1D) line or 2D plane. Such portions have been assumed to be representative of the whole astrocyte Ca²⁺ activity. This is, however, dubious given the highly 3D nature of astrocytes and of their relations with neighboring vascular and neuro-

nal elements, as well as the emerging complexity of astrocytic Ca²⁺ activity (2).

The reported potential feasibility of 3D two-photon Ca²⁺ imaging in astrocytes (27) and the recent availability of fast scanners and sensitive detectors led us to explore 3D scanning of entire astrocytes. By selectively expressing the genetically encoded Ca²⁺ indicator (GECI) GCaMP6f (28) in astrocytes, we succeeded in capturing whole-astrocyte Ca²⁺ activity, including in structurally unresolved regions (the so-called gliapil). We also addressed synapse-astrocyte interactions via expression of another GECI, jRCaMP1a (29), in neurons. Tens of gigabytes of 3D monitoring data were generated per acquisition and subjected to a dedicated analytical framework, providing a quantitative description of Ca²⁺ dynamics throughout a 3D astrocyte in both brain slices and awake mice.

Studies of astrocytes in two and three dimensions

Astrocytes have been studied via two-photon microscopy in a single horizontal plane (2D imaging). To quantitatively compare their morphological study in 3D versus conventional 2D imaging, we initially performed morphometric analysis of astrocytes in hippocampal slices from *GFAP-EGFP* mice (30) [*n* = 21; 7 from CA1, 6 from CA3, and 8 from dentate gyrus (DG)]. We acquired *z*-stacks containing the entire structure of individual astrocytes and extracted their morphology by software-assisted mask creation. Astrocytes appeared as structurally compact and optically resolved in their core regions (soma, stem processes with appendages ≥ 1 μm , endfeet) but “spongy” in their more peripheral regions, the gliapil, formed by fine branches and lamellae below optical resolution.

Therefore, we extracted volumes directly from fluorescence measures in the structural “core,” whereas we corrected measures done in the gliapil for volume fraction (30). The estimated average volume of an astrocyte was $13,019 \pm 1750 \mu\text{m}^3$ (range, 3000 to 35,000 μm^3), 25 \pm 2.5% of which was occupied by the structural core and 75 \pm 2.5% by the gliapil. Within the core, the soma occupied 22.5 \pm 2.2% of the volume, the stem processes with appendages 74 \pm 2.5%, and the endfeet 3.5 \pm 0.7%. On average, each hippocampal astrocyte had 3.5 endfeet (range, 1 to 7) and 5.8 stem processes (range, 3 to 9), and each process was 20.9 μm long (range, 5 to 64 μm) (Fig. 1). Astrocytes of the CA1, CA3, and DG regions were not significantly different in their volume measures (*P* = 0.76, 0.3, and 0.3 for total, core, and gliapil volume, respectively; Kruskal-Wallis test) and were therefore grouped in subsequent analyses.

Next, for a given astrocyte structure, we compared the structure volume visible in the best single two-photon focal plane (axial resolution, $\sim 1 \mu\text{m}$) (30) to the total structure volume. A single two-photon focal plane reported at maximum $4.0 \pm 0.30\%$ of the volume of a hippocampal astrocyte (Fig. 1 and movie S1). The best plane for endfeet reported 21.9 \pm 2.79% of the calculated endfoot volume and contained at maximum 2 of 3.5 endfeet. For the soma, the best plane reported 10.44 \pm 0.60% of its volume; for processes, the best plane reported 6.12 \pm 0.54% of their volume and contained 2.6 of 5.8 processes with an average length of 9.55 μm (range, 1 to 41.9 μm).

A 3D Ca²⁺ imaging and analysis approach for astrocyte studies

The above data prompted us to develop a 3D approach to studying astrocyte biology. We combined state-of-the-art technologies and new analytical methods (Fig. 2). For studying astrocyte Ca²⁺ dynamics, we generated double transgenic mice conditionally expressing GCaMP6f under the glial fibrillary acidic protein (GFAP) promoter (*hGFAPCreERT2xGCaMP6f* mice) (30). Analysis of GCaMP6f-positive cells in hippocampal slices from *hGFAPCreERT2xGCaMP6f* mice stained with antibodies to green fluorescent protein (GFP) (fig. S1) confirmed the astrocyte-specific expression of GCaMP6f in both the CA1 and CA3 regions (100% of GFP-positive cells double-positive for the astrocyte marker, glutamine synthase, and 0% for the neuronal marker, NeuN). In the DG, expression was 90% in astrocytes and 10% in other cells, most likely immature and newborn granule cells. GCaMP6f expression was homogeneous throughout the volume of individual astrocytes, including in the structurally unresolved gliapil region (fig. S1C). Astrocytes were also live-stained with the Ca²⁺-independent dye sulforhodamine 101 (SR101, 0.05 to 0.5 μM) (30). By combining SR101 and GCaMP6f maps, we obtained information for analysis of Ca²⁺ dynamics in both structurally resolved (core) and unresolved (gliapil) astrocyte regions and could detect movement artifacts, notably in vivo.

Our 3D imaging approach consisted of framing an isolated GCaMP6f-expressing astrocyte into a

Department of Fundamental Neuroscience, University of Lausanne, 1005 Lausanne, Switzerland.

*These authors contributed equally to this work.

†Corresponding author. Email: andrea.volterra@unil.ch

cuboid, the volume of interest (VOI), and rapidly acquiring images from its territory at a routine rate of about 2 Hz—that is, a rate of two full z -stacks (~60 focal planes) every second. Thanks to our advanced imaging apparatus (30) and the high signal-to-noise ratio (SNR) of GCaMP6f, at this speed we captured all the Ca^{2+} events of duration ≥ 1.5 s (FWHM, full width at half maximum amplitude) occurring in the selected VOI. Faster events (< 1.5 s) were visualized by increasing the acquisition rate in more restricted volumes (figs. S3, S5, and S8). Each of our imaging acquisitions generated data sets of several gigabytes. For their treatment we developed two complementary analysis methods, one optimized for analysis of Ca^{2+} events in structurally resolved regions [see also (14)] and another for analysis of Ca^{2+} activity in the absence of structural information, therefore in both the core and gliapil (Fig. 2) (30).

Distribution of Ca^{2+} dynamics in a 3D astrocyte and related problems of 2D imaging

At first, we quantitatively estimated the total Ca^{2+} activity in an entire astrocyte in basal condition. Activity detected during 3-min-long acquisitions in hippocampal astrocytes in situ (postnatal days 30 to 40; $n = 14$ cells, 5 in CA1 and 9 in DG) and expressed as mean voxel frequency (30) ($17,310 \pm 1591$ voxels per astrocyte; voxel size, $1 \mu\text{m}^3$) was

9.20 ± 1.34 mHz. Activity was distributed analogously in the structural core and gliapil; the percentage of activity in each compartment broadly matched its percentage volume (gliapil: 80% of activity, 75% of astrocytic volume; core: 20% of activity, 25% of volume). Total activity did not change in a second run ($P = 0.43$, signed-rank test), indicating that, macroscopically, astrocytic activity is stable over time and not influenced by laser scanning. Next, we calculated how much of the total Ca^{2+} activity detected in 3D is reported by 2D imaging. We subdivided the 3D map of total Ca^{2+} activity in each astrocyte into a z -stack of $1\text{-}\mu\text{m}$ -thick lateral planes, representing all the focal planes available in a conventional 2D two-photon acquisition (Fig. 3A), and expressed the total activity in each plane as a percentage of the total 3D activity. The best focal plane reported, at maximum, $11.4 \pm 0.8\%$ of the total activity of an astrocyte (Fig. 3B and movie S2).

We then analyzed Ca^{2+} activity in the structural core of the astrocyte, where we could define and characterize individual Ca^{2+} events. Of 666 events detected during 3D acquisitions from 15 cells, 567 (85.2%) occurred in processes, 65 (9.7%) in endfeet, and 34 (5.1%) in the soma (Fig. 3, C and D; mean event features in table S1). According to our estimations, 61% of such events would have been missed, and the remaining 39% incorrectly reported, in conventional 2D imaging experiments (fig. S2).

We next considered undersampling of the Ca^{2+} activity. The 2-Hz rate used here in 3D is within the range used in most 2D studies and represents the best compromise for imaging entire astrocyte activity with our system. Nonetheless, astrocytic activity was reported to also comprise fast events with FWHM ≤ 1.5 s (14, 31, 32), which would not be correctly captured at 2 Hz. Therefore, in some experiments, we restricted the 3D sampling volume to increase acquisition speed. We selected VOIs of eight focal planes centered on either an astrocytic process or one or multiple endfeet, including the surrounding gliapil, and compared event detection at 2 and 10 Hz. Faster scanning captured more Ca^{2+} events, resulting in an event frequency increase by a factor of 4.9 in processes ($n = 8$ processes in 4 cells) and by a factor of 5.4 in endfeet ($n = 13$ endfeet in 4 cells), respectively (figs. S3, S5, and S8). In particular, a new population of fast events appeared at 10 Hz (see below).

Distribution of Ca^{2+} dynamics in 3D astrocytes in awake mice

Next, we investigated astrocytes in vivo, in the somatosensory cortex of adult awake mice. Morphological analysis of the astrocytes in the somatosensory cortex did not show any significant difference with respect to hippocampal astrocytes, except for a higher number of endfeet per cell, 5 (range, 4 to 7) versus 3.5 ($P = 0.03$, rank sum test;

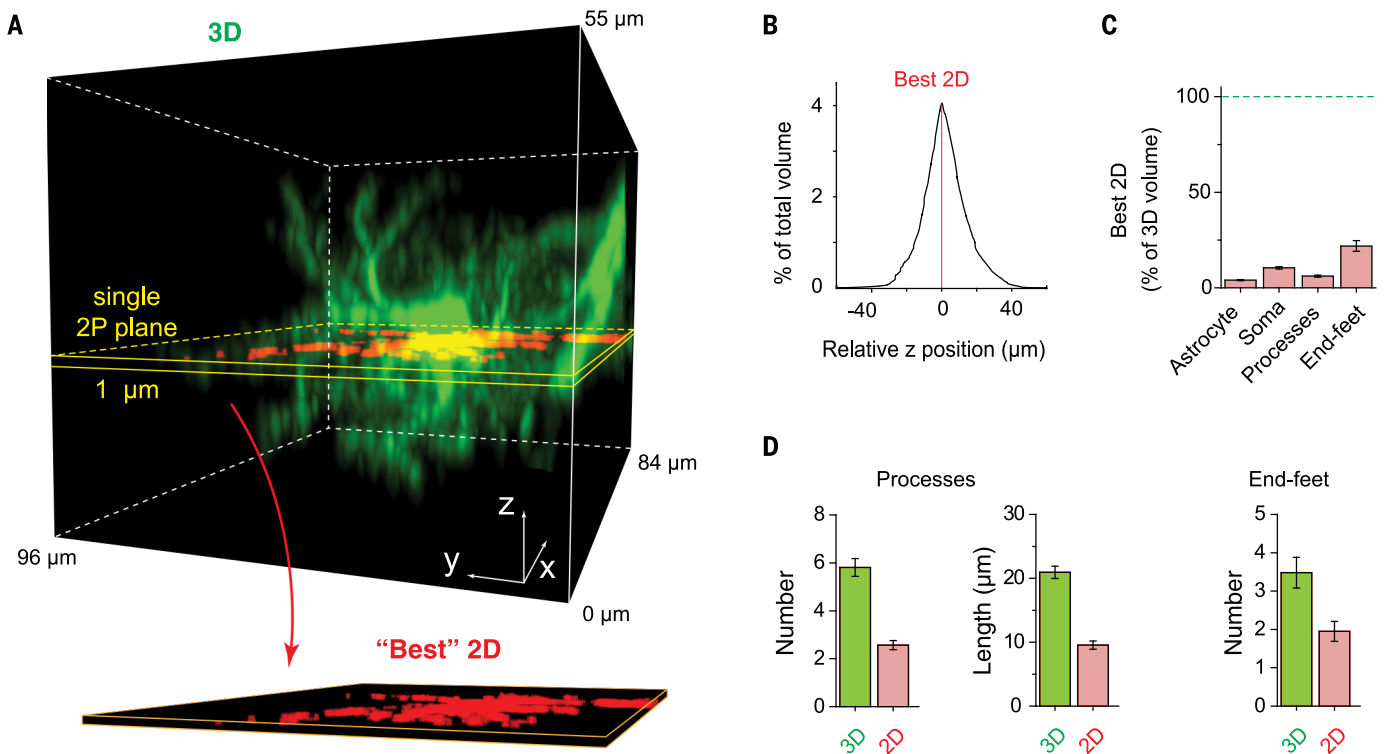


Fig. 1. Gray matter astrocytes are 3D cells poorly covered by 2D imaging. Comparative analysis of astrocyte morphology captured by 3D versus 2D two-photon imaging (*GFAP-EGFP* mice, $n = 21$ cells). “Best 2D” focal planes (FP, $z = 1 \mu\text{m}$) were those containing the maximum of astrocytic fluorescence. (A) Representative 3D stack of an EGFP-expressing astrocyte (top, green) and corresponding best

2D FP (bottom, red). (B) Graph showing percentage of astrocytic volume collected in each 2D FP relative to best FP. See also movie S1. (C) Histograms show percentage of astrocytic (or specific region) volume contained in best 2D FP. (D) Maximum number of processes or endfeet and maximal process length captured by best 2D FP versus 3D. All data are shown as means \pm SEM.

$n = 21$ hippocampal cells, 6 somatosensory cortex cells). We then performed 3D Ca^{2+} imaging, combining simultaneous camera tracking of the mouse movements (movie S3), and initially estimated the total Ca^{2+} activity in individual astrocytes. Mean voxel frequency was 22.73 ± 2.74 mHz ($n = 9$ cells; Fig. 3C), significantly higher than in hippocampal astrocytes ex vivo (+147%; $P = 0.0002$, Mann-Whitney test). This enhanced frequency was a feature of the in vivo condition, not of the brain area studied or of the age of the mice. Thus, in slices of 4-month-old mice, mean voxel frequency in somatosensory cortex astrocytes was 8.48 ± 2.05 mHz ($n = 3$ cells), significantly lower than in vivo (-63%; $P = 0.018$) and analogous to the frequency in hippocampal slices of younger mice ($P = 0.99$). High activity in vivo depended on the awake state, as activity in mice under isoflurane anesthesia dropped to 3.87 ± 1.31 mHz ($n = 3$ cells), only 17% of the activity of awake mice ($P = 0.009$) and <50% of the activity in astrocytes of brain slices ($P = 0.028$).

Visually, activity in awake mice was high in both the structural core and gliapil and occurred with faster dynamics than ex vivo. Thanks to

motion correction (30), we could count individual Ca^{2+} events in the structural core and further analyze part of them. Of 740 events detected in nine cells, 543 involved the processes (73.4%), 176 involved the endfeet (23.8%), and 21 involved the soma (2.8%). Their normalized frequencies, when compared to those ex vivo (30), gave in vivo/ex vivo ratios of 3.18 for endfeet ($P < 0.0001$, rank sum test), 1.82 for processes ($P = 0.0016$), and 1.17 for soma ($P = 0.19$; Fig. 3C).

3D Ca^{2+} activity in astrocytic processes

We then performed in-depth analysis of Ca^{2+} activity in the different core structures. We started with astrocytic processes in situ ($n = 72$ processes from 14 hippocampal astrocytes). Average activity was different in different processes, ranging from 0 to 14 mHz (mean voxel frequency; Fig. 4A), with 71% of processes showing low activity (0 to 3 mHz), 19% medium activity (3 to 6 mHz), and 10% high activity (>6 mHz). These levels were broadly stable in repeated acquisitions (fig. S4A). In most astrocytes, combinations of poorly active and more active processes were observed (Fig. 4A). Moreover, different processes were differ-

ently sensitive to the neuronal activity blocker tetrodotoxin (TTX; 1 μM): 48% of them showed strong Ca^{2+} event reduction (>75%), 24% only partial reduction (25 to 75%), and 28% no reduction ($n = 21$ processes in 5 cells; Fig. 4B). We then analyzed process activity in awake mice (60 processes from nine cortical astrocytes). Overall, processes in vivo were more active than processes ex vivo (maximal process activity, 28 versus 14 mHz), but, like processes ex vivo, showed heterogeneous levels of activity (12% low activity, 37% medium activity, 52% high activity) and combinations of more and less active processes in the same astrocyte.

We next analyzed Ca^{2+} activity distribution within individual processes. By averaging data from 72 processes in situ, we extracted values for mean voxel frequency per process volume (fig. S4B). In an “average” process, the largest volume fraction (>40%) contained very low or no activity (≤ 3 mHz). As the activity increased, the volume occupied was less and less, reaching <1% at frequencies of >30 mHz. This suggests the presence of small hot spots. Indeed, analysis of the 17 most active processes showed heterogeneous alternation of hot and cold spots along the processes

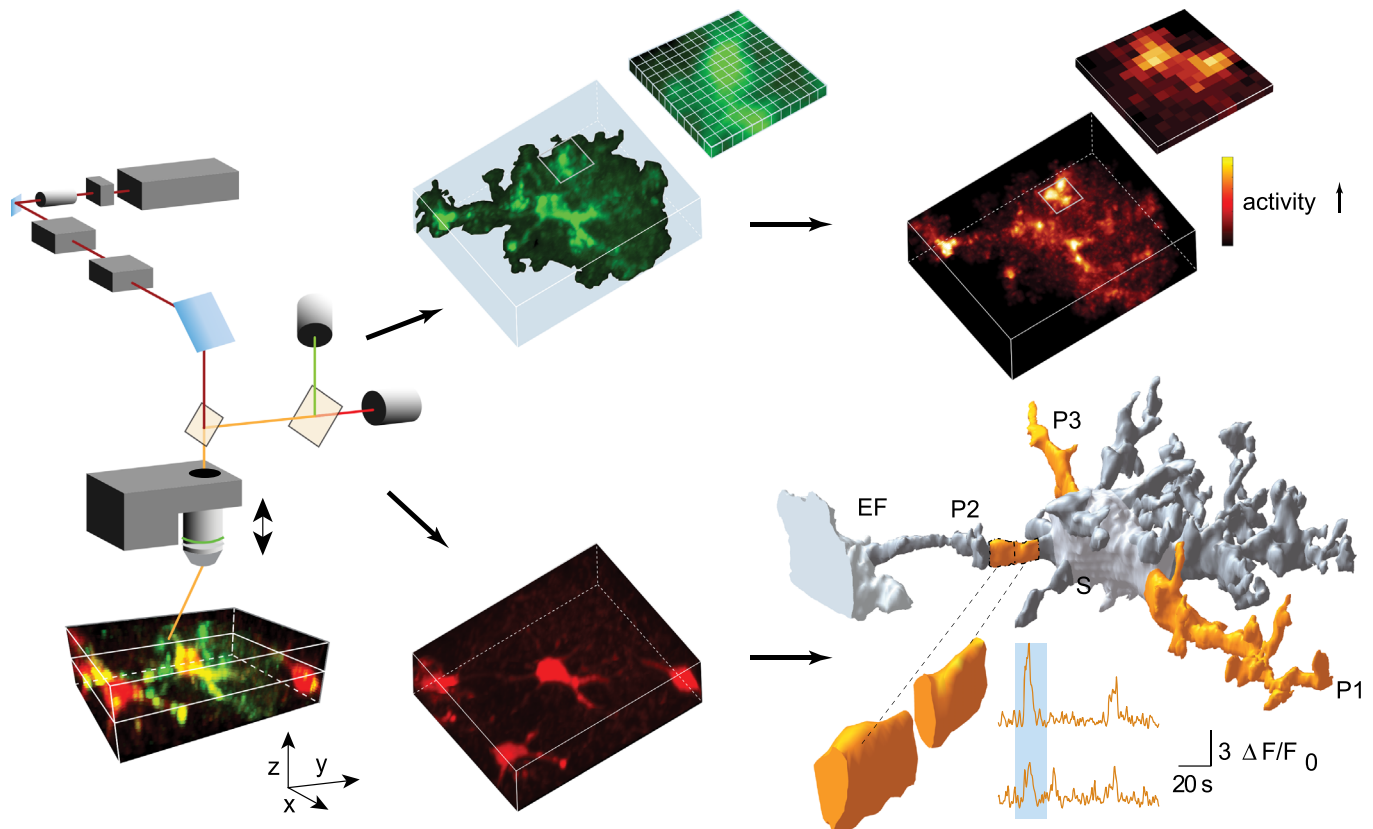


Fig. 2. A 3D imaging and analysis approach to study Ca^{2+} dynamics in entire astrocytes. Left: Entire astrocytic volumes [~ 30 focal planes (FP)] were routinely imaged at 2 Hz using a two-photon apparatus equipped with fast scan head, piezo-actuated objective, and high-sensitivity GaAsP detectors (morphology, SR101, red; Ca^{2+} , GCaMP6f, green). Left, top: Ca^{2+} activity (green) was analyzed voxel-by-voxel with the “structure-free method” (30), producing a 3D voxel-frequency map (yellow, highly active voxels) in both structurally resolved (core) and

unresolved (gliapil) astrocytic regions. Right, bottom: SR101 fluorescence signal (red) was used to segment the astrocyte core (gray) and identify individual compartments (S, soma; P1, P2, P3, processes; EF, endfeet). These were further subdivided into subregions (30). A snapshot of simultaneous Ca^{2+} activity in the three processes is shown in orange; the bottom fly-out shows two P2 subregions (19.4 and 8.8 μm^3 , respectively) and their corresponding Ca^{2+} traces. Blue shading indicates the period when P1, P2, and P3 were simultaneously active.

(Fig. 4, C and D). The “hottest” and “coldest” spots in a process were $1.5 \pm 0.3 \mu\text{m}$ and $2.2 \pm 0.31 \mu\text{m}$ long, respectively, as measured from activity maps calculated in $1\text{-}\mu\text{m}$ increments (30). No evident trend for associating these spots to specific process regions emerged.

Some of the Ca^{2+} events generated in processes reached the border with the somatic region, defined by the $3\text{-}\mu\text{m}$ -long subregion that we segmented at the interface between the two compartments. Only 22% of such events crossed the border and invaded the soma, whereas 78% stopped at the border ($n = 98$ events). A few experiments at higher acquisition speed (10 Hz) better delineated the characteristics of “crossing” versus “stopping” events ($n = 10$ and 65, respectively; fig. S4C). Relative to stopping events, crossing events were of longer duration by a factor of 4.10 ($P = 0.0019$, unpaired t test) and higher amplitude by a factor of 1.52 ($P = 0.048$, unpaired t test) ($n = 7$ crossing events, 21 stopping events). Experiments at 10 Hz also confirmed that process activity ($n = 216$ events in 8 processes) is largely local (mean event size, $40.50 \pm 3.11 \mu\text{m}^3$, corresponding to $12.49 \pm 1.11\%$ of the process volume) and enriched in fast events (FWHM, 0.68 ± 0.3 s), hence difficult to capture in 2-Hz acquisitions (see fig. S5).

3D Ca^{2+} activity in the somatic region

We then investigated the astrocytic Ca^{2+} events involving the somatic region in both hippocampal slices and awake mice. Analysis was restricted to events that could be correctly extracted (29 events from 14 cells in situ, 11 events from 9 cells

in vivo). For several events in vivo, parameters could not be correctly defined because animal movement caused the areas of interest to be out of focus during acquisition. In astrocytes of hippocampal slices, events involving the soma were highly heterogeneous and spread spatially over a vast range of volumes, from tens of μm^3 to $\sim 3000 \mu\text{m}^3$ (Fig. 4E). Part of them were relatively small ($\leq 300 \mu\text{m}^3$), mostly confined to the soma itself or resulting from activity in a proximal stem process invading the soma, often just partially. Others were larger and expanded to the whole somatic region plus additional connected structures, such as part or all of one or multiple stem processes and the surrounding gliapil. The volume of an event and its duration seemed to be related, with the largest events being the longest-lasting ones (Fig. 4E). We never observed in slices a somatic event that spread throughout the astrocytic core.

Relative to events ex vivo, events in vivo had faster kinetics and a larger range of volumes: $\sim 890 \mu\text{m}^3$ to $10,000 \mu\text{m}^3$ (average, $4470 \pm 1051 \mu\text{m}^3$; Fig. 4E). Some of these events expanded to volumes similar to those of the largest events ex vivo, but others were much larger (mean volume, $6375 \pm 1106 \mu\text{m}^3$; $n = 7$ events) and involved the whole structural core of the astrocyte and a good part of the surrounding gliapil. We called this new class the “global” events. They appeared to originate at several unrelated foci, generally in the gliapil, and from there to expand to the rest of the astrocyte (Fig. 4F and fig. S6). Of the seven global events observed, six occurred in temporal correlation (delay of onset, 1 to 3 s) with animal

locomotion (movie S3). No global events were observed in anesthetized mice lacking locomotion.

If global events depend on intense neuronal discharge associated with movement (33), it seems logical that we did not see them in hippocampal slices displaying only sparse neuronal firing (14). To artificially increase neuronal discharge in the slices, we applied the pro-epileptogenic drug 4-aminopyridine (4-AP, $100 \mu\text{M}$) and monitored local field potentials (LFPs) while performing 3D Ca^{2+} imaging in astrocytes (30). Within 10 min, 4-AP induced a regular series of large LFPs, representing events of hypersynchronous neuronal discharge (34). In temporal correlation (delay, ≤ 2 s), we always observed a “global-like” Ca^{2+} event in the monitored astrocyte, much larger than all the somatic events recorded in basal conditions ($3099 \pm 296 \mu\text{m}^3$, $n = 7$; fig. S7).

3D Ca^{2+} activity in endfeet and related processes

We next analyzed Ca^{2+} activity involving astrocytic endfeet. SR101-based segmentation revealed the presence of multiple endfeet per astrocyte, although sometimes we could hardly define their exact borders and number. To obtain more precise morphological information, we performed parallel studies in fixed slices of *GFAP-EGFP* mice labeled with the endfoot-selective marker Aquaporin-4 (AQP-4; Fig. 5A). Often two endfeet, stemming from different processes or from two branches of the same process, enwrapped contiguous segments of the same blood vessel. Less frequently, two endfeet enwrapped noncontiguous segments or

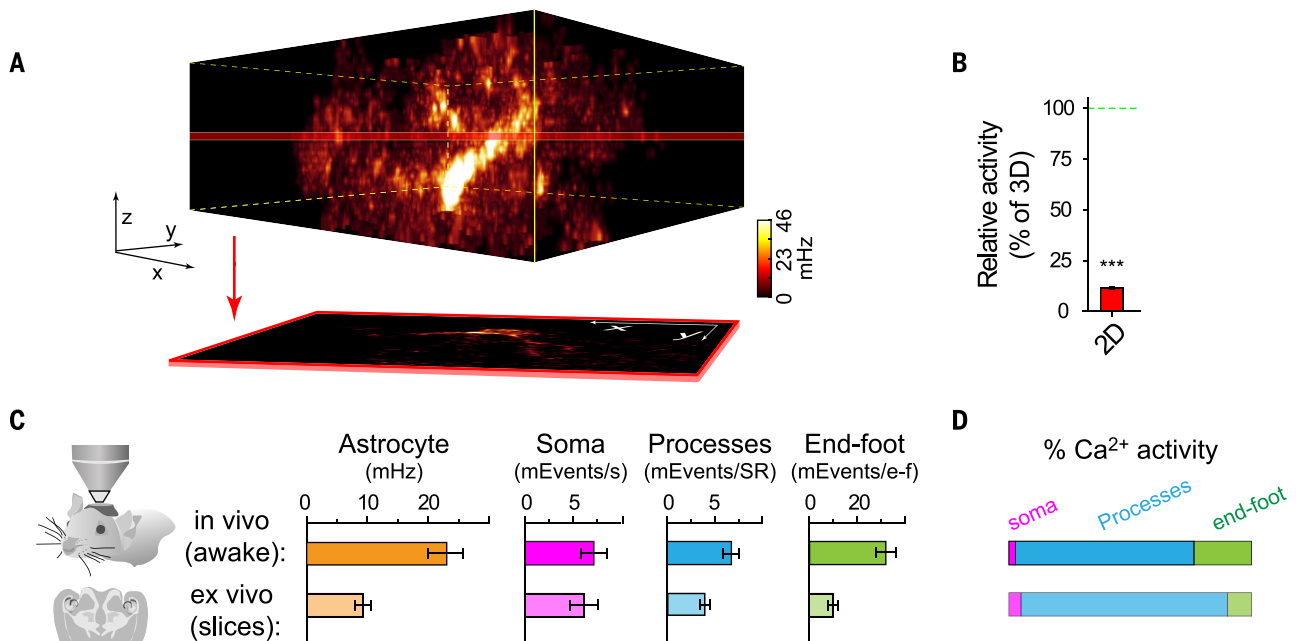


Fig. 3. 3D astrocytic Ca^{2+} activity in vivo and ex vivo: Comparison with 2D. (A) Representative 3D voxel-frequency map (and corresponding best 2D FP) of a hippocampal astrocyte in situ (VOI = $57 \mu\text{m} \times 44 \mu\text{m} \times 21 \mu\text{m}$). Color scale indicates voxel activity. (B) Group data from 14 cells showing percentage of total 3D detectable activity captured by best 2D FP. See also fig. S2 and movie S2. $***P < 0.00001$. (C) Comparison

of Ca^{2+} activity detected in cortical astrocytes from awake mice (top row) and in hippocampal astrocytes from acute slices (bottom row). Data are mean voxel frequencies in the entire astrocyte or normalized event frequencies in each compartment. (D) Ca^{2+} activity distribution (in percentage) among soma, processes, and endfeet [color code as in (C)]. Data in (B) and (C) are expressed as means \pm SEM.

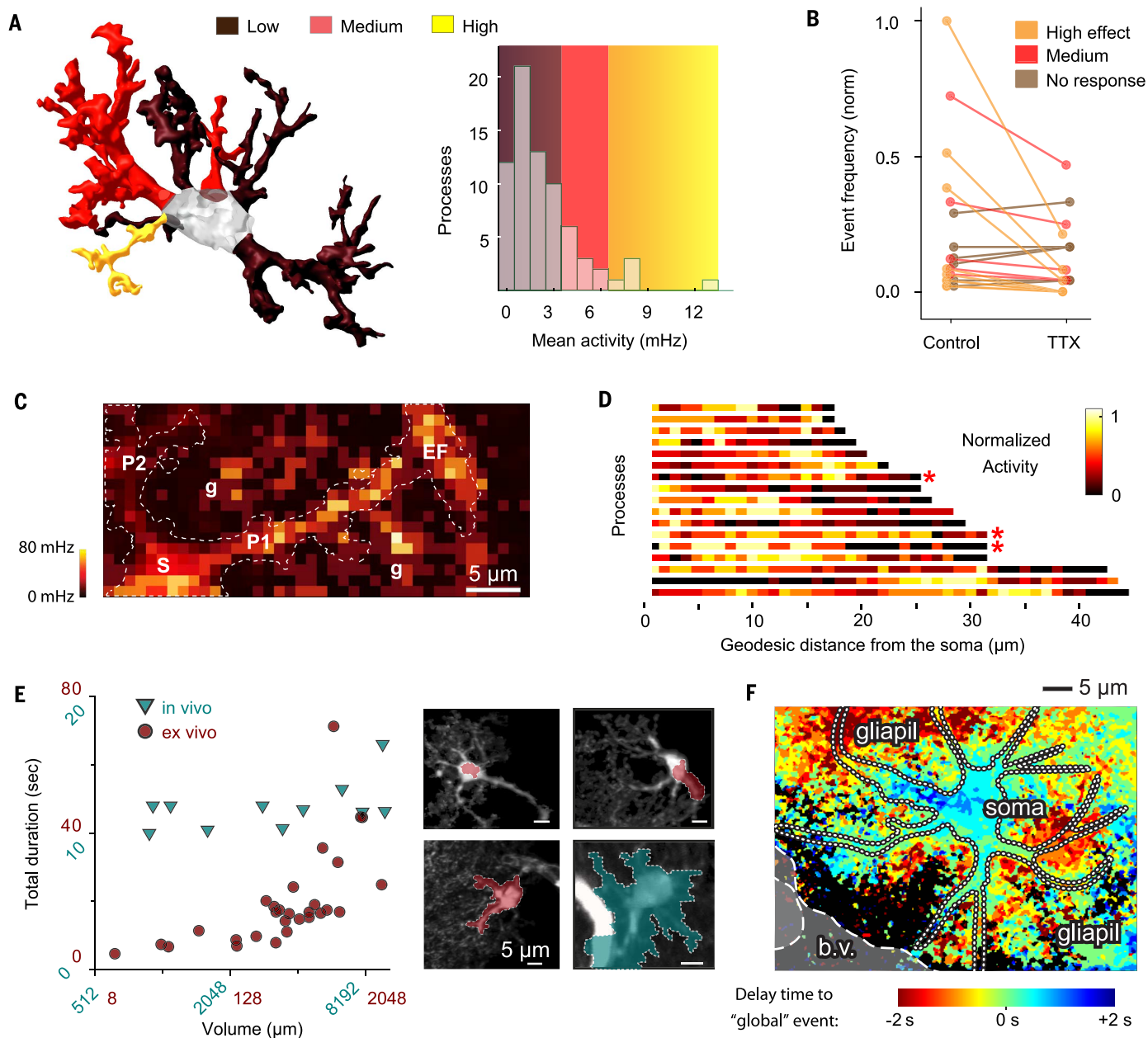


Fig. 4. Astrocytic Ca^{2+} activity in processes and soma is highly heterogeneous. (A) Left: 3D reconstruction of a hippocampal astrocyte in situ (core structure); processes are color-coded according to average activity level. Right: Distribution of all processes from recordings in situ ($n = 72$) based on individual mean Ca^{2+} activity. See also fig. S4, A and B. (B) Effect of TTX on basal Ca^{2+} activity in individual processes in situ ($n = 21$); color coding highlights different levels of inhibition (high, >75%; medium, 25 to 75%; no, <25%). (C) Voxel activity map showing microscopic heterogeneity of Ca^{2+} activity within each process and surroundings (P1 and P2, processes; S, soma; EF, endfoot; g, gliapil; voxel size, $1 \mu\text{m}^3$). Note the hot spots (yellow) and cold regions (brown) along the process. (D) Distribution of local Ca^{2+} activity within each individual process versus distance from soma

($n = 17$ medium- and high-activity processes). Activity was calculated voxel-by-voxel (size, $1 \mu\text{m}^3$) and normalized to maximal activity in the process. Asterisks denote endfoot-related processes. (E) Left: Distribution of spatial spread versus total duration (semilogarithmic scale) of Ca^{2+} events involving the astrocytic soma (ex vivo, $n = 29$; in vivo, $n = 11$; symbol and scale color code: in vivo, teal; ex vivo, maroon). Right: Representative examples of spatially heterogeneous somatic events overlaid on the astrocytic morphology (red, ex vivo; green, in vivo). See also fig. S4C. (F) Temporal cross-correlation projection map (30- μm stack) of GCaMP6f activity indicating multifocal origination of a global event in vivo; "lead" voxels (shades of red) precede the main event cluster at the astrocyte periphery, mainly in the gliapil. Core structure is outlined; b.v., blood vessel. See also fig. S6.

segments of two different vessels. Rarely ($\leq 20\%$ of cases), two endfeet were fully contained in a single focal plane.

Functional analysis was performed on 86 Ca^{2+} events from 17 astrocytes ex vivo and 174 events from 9 astrocytes in vivo. Despite the much higher frequency in vivo (Fig. 3C), events in the two conditions displayed similar spatial spread: The majority stayed confined to the endfoot domain itself (62% ex vivo, 53% in vivo; Fig. 5C), whereas others involved both the endfoot and connected process (35% ex vivo, 24% in vivo). Events expanding beyond the endfoot process were just 3% ex vivo. They reached 22% in vivo, but mostly as part of

global astrocytic events. In a few recordings at 10 Hz with VOI centered on endfeet, we observed an additional population of events (fig. S3). They were fast (FWHM, 0.75 ± 0.03 s) and highly spatially restricted, occupying just fractions of the segmented endfeet, on average $16.32 \pm 1.50\%$ of a single endfoot volume (96 of 136 events in 13 endfeet; see fig. S8).

Simultaneous monitoring of activity in two or more endfeet showed preponderant asynchronicity (81% of cases ex vivo, $n = 52$ events; 58% in vivo, $n = 92$ events; Fig. 5B). Enhanced synchronicity in vivo was mainly because of global events, which generally coordinate all the astrocytic Ca^{2+} activity,

not only endfoot activity. Another more local type of synchronicity involved two endfeet enwrapping contiguous segments of the same blood vessel and their associated endfoot processes (Fig. 5B). According to current views, endfoot processes should form a “functional unit” with related endfeet. Thus, each endfoot process would function as an “axonlike highway” conveying all the network-related information sensed by an astrocyte to its respective endfoot for coordinate control of local blood flow (5). Contrary to this idea, we found that endfoot processes and related endfeet were often independently active; in only 23% of cases in vivo and 30% ex vivo did they show coordinated

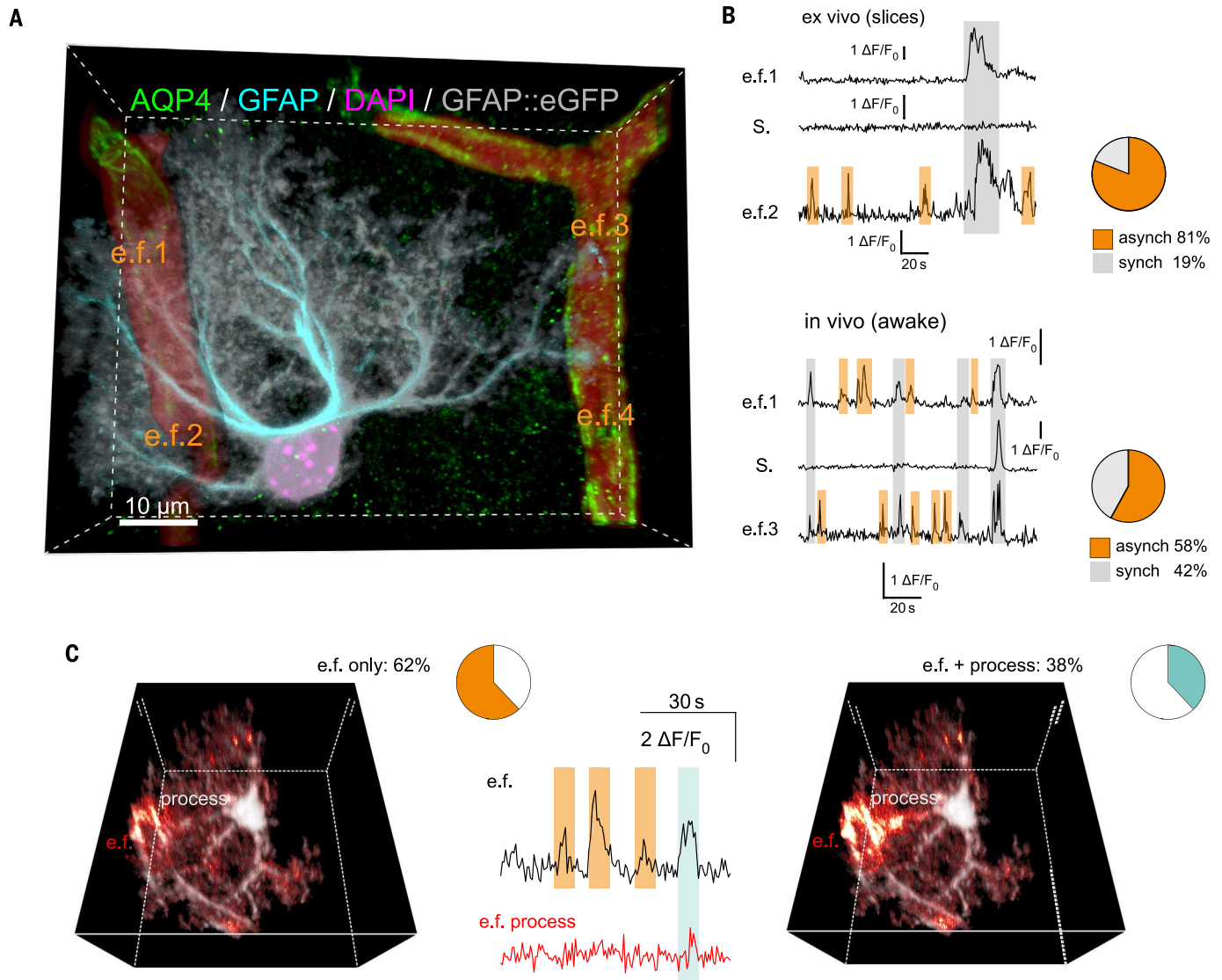


Fig. 5. Endfeet of the same astrocyte are independently active but occasionally show local or global coordination. (A) Confocal 3D stack ($z = 33 \mu\text{m}$) of a hippocampal astrocyte from a *GFAP-EGFP* mouse. Endfeet (e.f. 1, 2, 3, 4) and processes are identified by GFAP staining (cyan), red blood vessel outline by AQP4 (green), and nucleus by 4',6-diamidino-2-phenylindole (DAPI; magenta). (B) Representative Ca^{2+} traces showing activity in two endfeet of the same astrocyte. Top: Ex vivo [e.f. 1 and 2 refer to organization in (A)]. Bottom: In vivo (e.f. 1 and 3). Orange shaded areas denote asynchronous

events; gray shaded areas denote synchronous events, mostly independent of somatic (S) Ca^{2+} elevation, except one in vivo, part of a global event. In the scale bar, $\Delta F/F_0$ denotes change in fluorescence over the baseline (average fluorescence). (C) Two-photon snapshots (VOI = $56 \mu\text{m} \times 49 \mu\text{m} \times 31 \mu\text{m}$) showing examples of Ca^{2+} activity in a hippocampal astrocyte either confined to an endfoot (e.f., left) or also involving the related process (e.f. process, right). Corresponding traces and distribution pie charts show the former and latter cases in orange and green, respectively.

activity. Moreover, endfoot processes displayed mostly local activity, not different on average from that in other processes (mean voxel frequency, other processes versus endfoot processes: *ex vivo*, $P = 0.32$; *in vivo*, $P = 0.83$; rank sum test).

3D imaging reveals local axon-astrocyte functional interactions

Next, we investigated the structural and functional 3D relations between axons and astrocytes in hippocampal slices from adult mice. For morphological studies, we virally injected the red reporter tdTomato in neurons of layers II and III of the entorhinal cortex (EC) of *GFAP-EGFP* mice (fig. S9 and movie S4); for functional studies, injections were made in *GFAPCreERT2αGCaMP6f* mice. Thereby we highlighted a dense meshwork of fluorescent axons corresponding to medial and lateral perforant path (PP) fibers (Fig. 6A).

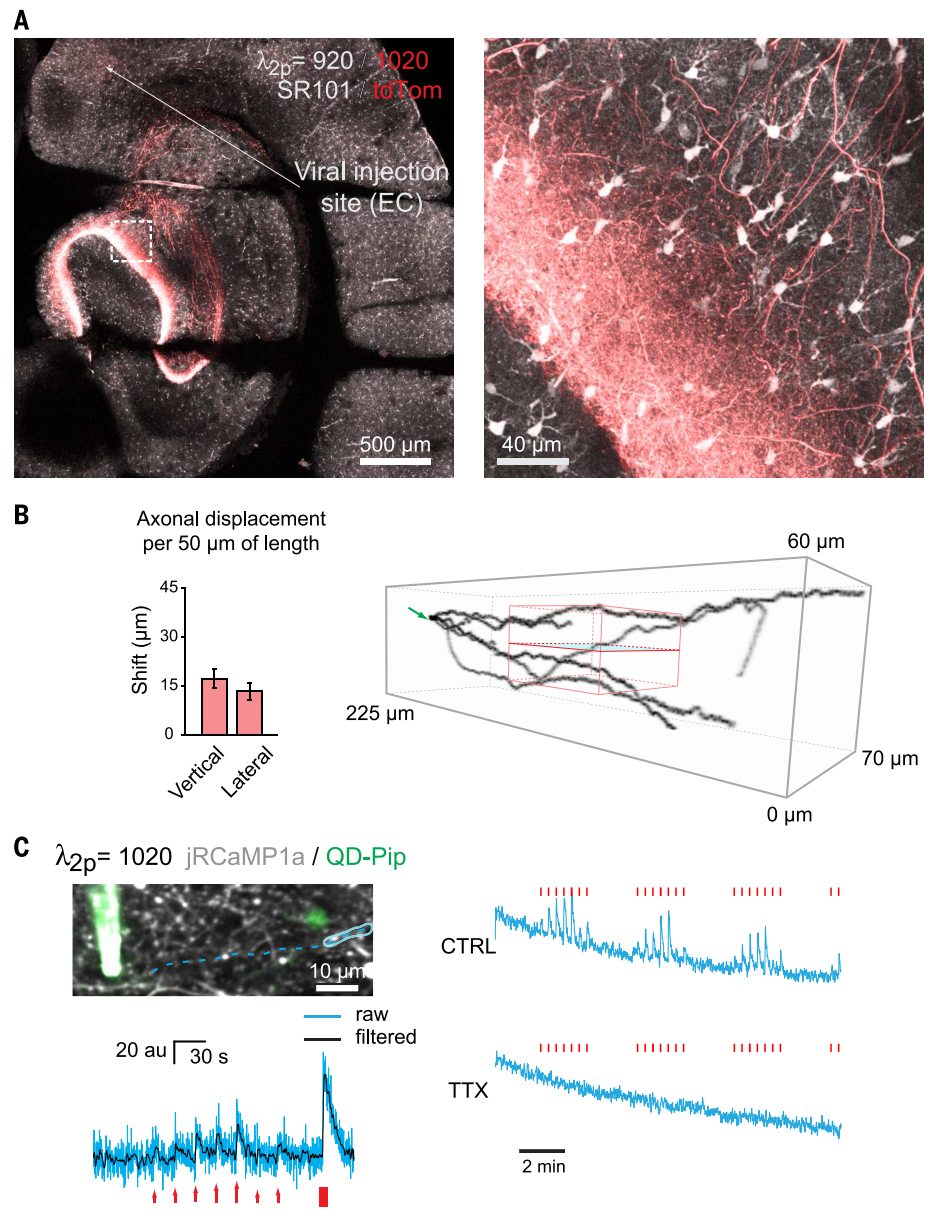
Fig. 6. Hippocampal axons have complex 3D morphological interactions with astrocytes: A functional study with 3D Ca^{2+} imaging.

(A) Axonal tracing experiment to study axon-astrocyte interactions. Perforant path (PP) axons (red) are highlighted upon viral injection of red fluorescent tdTomato in entorhinal cortex (EC); astrocytes are highlighted upon loading with SR101 (white). Left: Large view of the fluorescent axonal fibers in the hippocampal formation. Right: Close-up of the boxed region at left, showing arrival of PP axons in the lateral and medial dentate molecular layers and their complex intermingling with astrocytes. See also fig. S9. **(B)** Left: Histograms showing mean lateral and vertical deviation of fluorescently labeled PP axons (length followed: $108 \pm 15 \mu\text{m}$, range 32 to 251 μm ; $n = 20$ axons). Right: 3D reconstruction of five axons from the same slice artificially aligned to the start point (green arrow) to visualize 3D deviations. The red box represents a typical astrocytic VOI imaged in our 3D Ca^{2+} experiments; shown in cyan is an individual 2D focal plane. The box, but not the plane, contains most of the axonal deviations and is therefore appropriate to study axon-astrocyte functional interactions. See also movie S4. Group data are shown as mean \pm SEM. **(C)** Targeted axonal electrical stimulation causes reliable Ca^{2+} increase detectable in a single fiber expressing the red GEC1, jRCaMP1a. Top left: Setting for axonal stimulation experiments, showing quantum dot-coated (QD) fluorescent tip of stimulating pipette, axonal fiber of interest (blue dotted line) and ROI (blue) along the axonal path from which we recorded Ca^{2+} signals. Bottom left: Trace of graded Ca^{2+} increases in the ROI upon one to five brief electrical stimulations (red arrows: 50 Hz; interpulse interval, 20 s). At the end, a larger Ca^{2+} elevation is induced by tetanic stimulation (red block, 100 pulses at 100 Hz). Blue trace, raw jRCaMP1a data; black trace, data filtered with Gaussian filter ($\sigma = 0.5$ s, two-photon excitation wavelength $\lambda = 1020$ nm). Right: In a different experiment, the average Ca^{2+} trace from several activated fibers shows stable response to repetitions of the above protocol at 2- to 3-min intervals ($\lambda = 965$ nm). This response is fully blocked by TTX (1 μM).

Such fibers contain recurrent varicosities (inter-distance, 3 to 20 μm) making excitatory synapses mainly onto dendritic spines of granule cells (GCs) in the outer two-thirds of the dentate molecular layer (35). PP axons did not keep horizontal trajectories along their paths; rather, they deviated significantly both laterally and vertically (see Fig. 6B) and crossed astrocytic territories in a highly 3D manner. Reconstruction of five such axons artificially aligned at the starting point of the monitored tract shows that axon-astrocyte interactions are comprehensively captured by 3D but not conventional 2D scanning (Fig. 6B). Therefore, 3D Ca^{2+} imaging is appropriate to answer whether astrocytes respond to minimal axonal stimulation, as reported by some studies (14, 15) and contradicted by others (24, 26).

To address this question, we selected an axon stimulation protocol known to evoke minimal synaptic activation in dentate GCs (14, 36). The protocol consisted of a ramp of one to five pulses of 30- μA current delivered at 50 Hz, spaced by 20-s intervals to avoid induction of any synaptic plasticity. Sometimes at the end we applied a tetanic stimulation (100 pulses at 100 Hz) to assess maximal response. To visualize PP axonal activity and confirm minimal stimulation, we virally transfected layer II and III EC neurons with the red Ca^{2+} indicator jRCaMP1a (29). Fluorescent PP axons were focally stimulated via the tip of a quantum dot-coated patch-pipette (QD pipette, 540 nm) (30) (Fig. 6C), and Ca^{2+} activity was monitored in a VOI traced along the visible axonal fiber tracts proximal to the QD pipette. The above protocol elicited a series of distinct Ca^{2+} signals with peaks of increasing amplitude proportional to the number of pulses in the ramp (Fig. 6C). Even single-pulse stimulations, representing individual

Downloaded from <http://science.sciencemag.org/> on May 24, 2017



action potentials, produced a jRCaMP1a signal in the axons. Repetition of the ramp at 20-s intervals induced a highly reproducible pattern of small axonal Ca^{2+} responses, which were abolished in the presence of TTX (1 μM). Tetanic stimulation at the end of the ramp produced a Ca^{2+} signal of much higher amplitude (Fig. 6C).

We then examined the astrocytic responses to such stimulations. We selected a tdTomato-fluorescent axon passing in the territory of a GCaMP6f-expressing, SR-101-loaded astrocyte (Fig. 7A and fig. S9C) and positioned the stimulating QD pipette proximal to it and $\geq 40 \mu\text{m}$ away from the astrocytic territory to avoid any direct astrocyte activation. We applied minimal axonal stimulation protocols spaced by intervals of no stimulation (2 to 3 min) and simultaneously recorded Ca^{2+} activity throughout the 3D astrocyte volume (Fig. 7, A and B; $n = 12$ experiments). Using post hoc cumulative cross-correlation analysis (30), we identified the Ca^{2+} activity time-locked to axonal stimulation in the midst of all the endogenous astrocytic activity, and could build 3D maps of the astrocytic regions displaying axonal firing-related activity. We called these regions “reliably responding regions” because they consistently responded to all the stimuli in the protocol, even the single pulses (Fig. 7A).

Often minimal in size ($60.7 \pm 24.3 \mu\text{m}^3$; Fig. 7B), responding regions were generally positioned in the gliapil, in the direct vicinity of the visible axon targeted with the stimulation pipette. In some cases, they were also at some distance, possibly due to concomitant stimulation of nonfluorescent axons. To verify the extent of overall axonal recruitment (fluorescent and nonfluorescent fibers), we monitored the postsynaptic Ca^{2+} responses evoked by our minimal stimulation protocol in GCs ($n = 3$; see also fig. S10). Responses were confined to a minimal fraction of the monitored neuropil volume, consistent with recruitment of a very limited number of axon fibers. Stronger stimulations activated a much higher neuropil fraction (fig. S10D).

To verify the robustness of our method for detecting astrocyte “responding regions,” we performed several controls: (i) We randomly selected VOIs in the astrocytic territory of the same size as the responding regions and checked their Ca^{2+} activity during the same acquisition period. Total activity in these VOIs was less than in responding regions and was mostly time-uncorrelated with axonal stimulations (Fig. 7, A and B; we called these regions “nonresponding regions”). (ii) Within reliably responding regions, we compared Ca^{2+} activity during equal periods of stimulation and nonstimulation. Activity largely clustered in the stimulation periods (fig. S11). (iii) We evaluated the TTX sensitivity of the astrocyte Ca^{2+} activity in responding and nonresponding regions. TTX suppressed Ca^{2+} activity only in responding regions ($-81 \pm 5.8\%$; $P < 0.05$, signed-rank test; $n = 6$ experiments; Fig. 7B and fig. S11C).

Finally, to directly demonstrate the cause-effect relation between axonal firing and astrocytic Ca^{2+} activity in responding regions, we performed dual-color GECI 3D Ca^{2+} imaging. In a few experi-

ments, we succeeded in simultaneously monitoring jRCaMP1a signals in axons and GCaMP6f signals in contiguous astrocytic regions ($n = 3$). Figure 7C shows temporally enlarged traces from one such experiment. A number of Ca^{2+} elevations are seen in the selected astrocytic region directly contiguous to the stimulated axonal fibers, each one time-correlated to the action potential-evoked axonal Ca^{2+} response present in the vicinity. Astrocytes responded even to the lower levels of stimulation in the ramp, including a single action potential pulse; however, not all the axonal Ca^{2+} elevations were accompanied by an astrocytic Ca^{2+} elevation, possibly because of synaptic failures associated with minimal stimulation (14). Both axonal and astrocytic Ca^{2+} elevations were blocked in the presence of TTX, directly demonstrating the action potential-dependent origin of the local astrocyte responses.

Discussion

We studied astrocyte Ca^{2+} dynamics in three dimensions, capturing all the Ca^{2+} activity in the volume of an astrocyte, including in response to axonal firing. Several aspects permitted this advance: (i) the capacity to map Ca^{2+} dynamics throughout the astrocyte, in both structurally resolved (core) and unresolved (gliapil) regions, in brain slices and in vivo, thanks to the use of an activity-independent indicator (SR101) delineating astrocyte morphology and controlling for movement artifacts, combined with a GECI (GCaMP6f) with high SNR and cellwide, astrocyte-specific expression; (ii) the capacity to scan the whole astrocytic territory at a routine rate of 60 different focal planes/s capturing all astrocytic Ca^{2+} events with duration ≥ 1.5 s, and to scan smaller but functionally relevant 3D domains (a process, one end-foot, or multiple endfeet) at a factor of 5 higher rate to also capture faster events (< 1.5 s); (iii) the capacity to study local 3D axon-astrocyte interactions, including with dual-color GECI imaging, and to resolve fine details of the respective activities, down to single action potential-related axonal Ca^{2+} transients and associated astrocytic Ca^{2+} spots; and (iv) the capacity to analyze data sets of tens of gigabytes per acquisition via in-house methods optimized for analysis of Ca^{2+} activity in the presence or absence of structural information.

As revealed by 3D imaging, Ca^{2+} activity is present throughout the astrocyte—including in structurally unresolved regions—and occurs mainly as a myriad of asynchronous local signals. The majority resides in the gliapil, which we estimated occupies $\sim 75\%$ of the cell volume. Within the smaller structural core, astrocytic processes are the region where Ca^{2+} activity is most frequent, followed by endfeet, particularly in vivo, whereas activity in the soma is infrequent (less than in processes by a factor of at least 20 to 30; see below). Passage of signals from region to region seems to be limited, possibly by barriers favoring regional compartmentalization. Even within individual compartments such as cell processes, activity is highly heterogeneous, and its level often differs greatly from process to process. Likewise, hot and cold spots alternate within individual processes.

Three-dimensional imaging is not only appropriate but also necessary for correct study of Ca^{2+} dynamics in astrocytes. To start, astrocytic Ca^{2+} activity is highly heterogeneous and mostly local, clearly indicating that “partial imaging” of an astrocyte, as necessarily done in 2D studies, is not representative of whole-cell activity. According to our volumetric calculations, conventional 2D two-photon Ca^{2+} imaging covers no more than 4% of the astrocyte volume and 11% of its activity (with confocal imaging, focal volume may be set larger by opening the pinhole, but this is still minimal relative to the total astrocytic volume). Likewise, 2D measures of activity in single astrocytic processes cannot be generalized to other processes, because simultaneous imaging of the different processes of an astrocyte shows a wide range of differences (up to a factor of 20) in their activities. Partial imaging in 2D often incompletely reports even individual Ca^{2+} events. Thus, events detected in a single horizontal plane are not necessarily restricted to that plane, and assuming that they are will often lead to erroneous description of their frequency and spatiotemporal characteristics (see fig. S2). Finally, PP-axon-astrocyte interactions are highly 3D and are unlikely to be correctly studied in 2D, particularly at low levels of axonal activity. Thus, astrocyte responses to minimal axonal stimulations appear as spotlike Ca^{2+} elevations that occupy $< 1\%$ of their volume and would be missed with 2D imaging, unless by chance they occurred in the selected focal plane. This observation could explain why some previous 2D studies could not detect astrocyte responses to low levels of axonal activity and concluded that astrocytes respond only to intense neuronal firing (26). The latter responses are much larger in volume (e.g., figs. S7 and S11C) and are likely to be seen in any randomly selected focal plane.

By performing 3D recordings in astrocytes from both brain slices and awake mice, we could directly compare the two conditions. Activity in vivo was faster and more frequent than in slices but was not crucially different in nature (mostly local and asynchronous) and cell distribution (mostly in processes, then in endfeet, and eventually in soma). Quantitatively, the most striking difference was the higher frequency (by a factor of 3) seen in endfeet in vivo. Qualitatively, we found a population of very large events in vivo, which we called global Ca^{2+} events, that spreads spatially to most of the astrocytic structures, including both the core and gliapil. Most of these events were seen upon movement of the mouse and could be part of the widespread, multiregion astrocytic activation associated with the startle response (37). Global events were not spontaneously present in brain slices, most likely because of the severing of projection fibers. Nonetheless, we could evoke global-like responses in slices by intensifying neuronal firing artificially via 4-AP administration or high-frequency stimulation. Use of isoflurane anesthesia strongly reduced astrocytic activity in vivo, down to levels much lower than in awake mice (-85%) or in brain slices (-55%), casting doubt on studies of astrocyte biology in vivo in anesthetized mice.

An emerging feature of astrocytic Ca^{2+} activity is compartmentalization. Only a tiny minority of the events seen in processes invaded the somatic region, and most of those that reached the interface stopped there. Likewise, for endfoot events, only a minority of them expanded to the related process and even fewer beyond it. This implies that some form of physical and/or biological barrier is present at the interfaces, such as a high concentration of buffering organelles or of soluble buffers operating as Ca^{2+} sinks. Local barriers could also be present within compartments and may account for the observed alternation of hot

and cold domains. In this respect, different astrocytic regions seem to differ in their resting Ca^{2+} level (38), and mobile mitochondria seem to operate along astrocytic processes as local Ca^{2+} buffers [(39), but see (40)]. Overall, an astrocyte could preponderantly function as an assembly of thousands of independent local units heterogeneously distributed both macroscopically and microscopically. Such heterogeneity could explain, for example, the different levels of activity observed in different processes of an astrocyte, or in different domains of an individual process, and their stability over time. Although the underlying biological

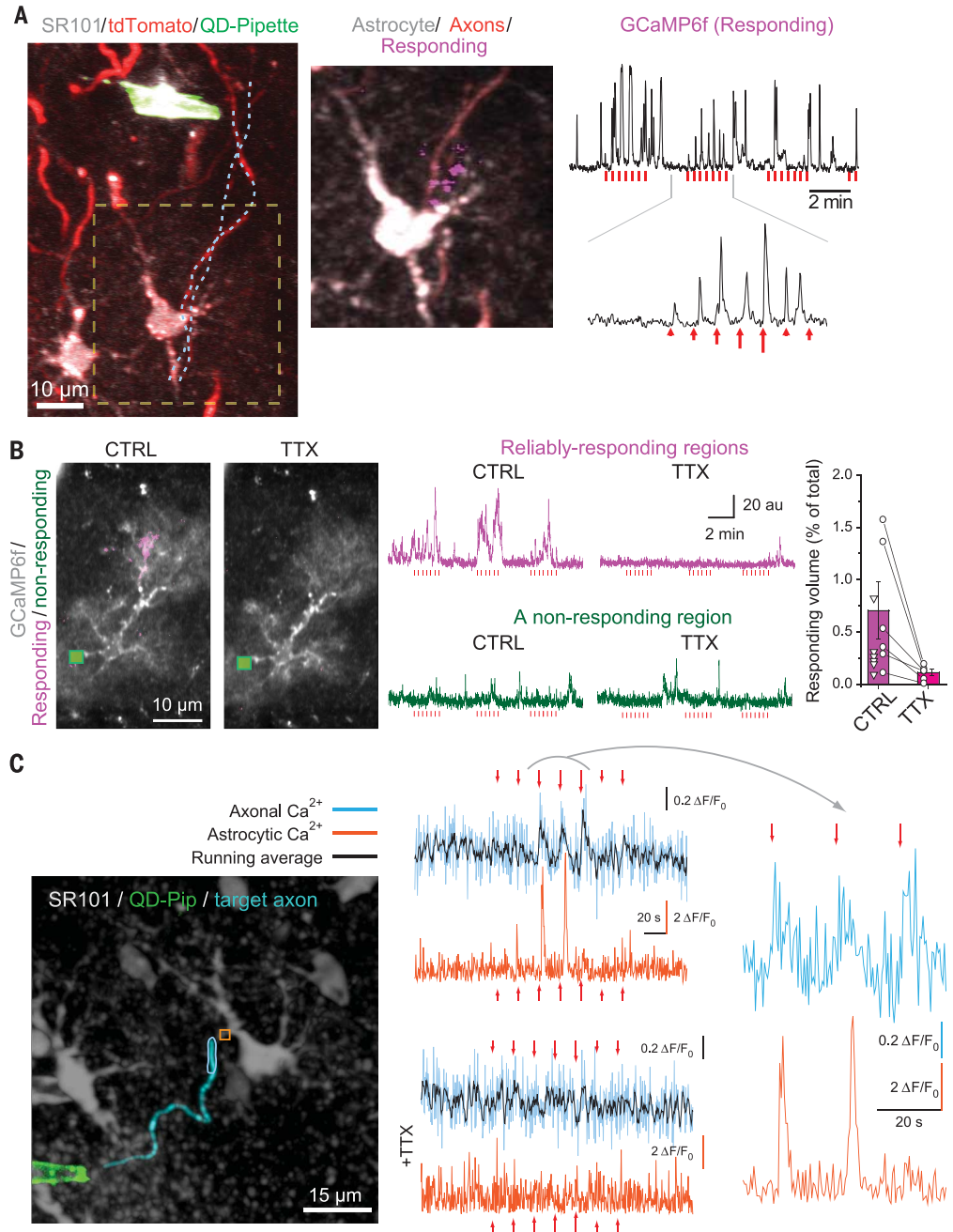
substrate remains to be defined, it might involve specific characteristics of the local microenvironment, including location and density of contacts with synapses; of receptors, channels, and other proteins starting Ca^{2+} signaling; or of internal organelles acting as Ca^{2+} sources and sinks. Functional units coordinate under specific circumstances, first more locally and then more macroscopically. Multicompartmental Ca^{2+} events are rather infrequent and probably need to possess “supra-threshold” characteristics to cross interfaces and carry information requiring intercompartmental coordination.

Fig. 7. Astrocytes detect and respond to minimal axonal stimulation in a small portion of their volume.

(A) Representative targeted axonal stimulation experiment. Left: QD stimulation pipette positioned $>40\ \mu\text{m}$ away from a GCaMP6f-expressing astrocyte and adjacent to tdTomato-labeled axons (blue dotted highlight) crossing the astrocytic territory. Center: Close-up of boxed region at left (z-projection of $20\text{-}\mu\text{m}$ stack). Magenta color coding highlights a computationally identified “reliably responding” region, displaying Ca^{2+} elevations temporally correlated to minimal stimulation of adjacent axons (protocol as in Fig. 6C). Right: 15-min trace of the astrocytic GCaMP6f signal extracted from the responding region. The close-up highlights astrocytic Ca^{2+} responses also to single action potential pulses (first and sixth arrows). See also fig. S9 and supplementary text regarding spontaneous activity in nonstimulation periods.

(B) Left: Effect of TTX on the region reliably responding to axonal stimulation (magenta). The green box denotes a nonresponding region of equal size, arbitrarily selected. Center: GCaMP6f traces extracted from a reliably responding region (magenta) and a nonresponding region (green) in control (CTRL) and TTX. TTX suppresses “evoked” Ca^{2+} responses in the responding region but does not visibly affect spontaneous activity in both regions. Right: TTX significantly reduces the astrocytic volume reliably responding to axonal stimulation (circles, $n = 6$; $P < 0.05$, Wilcoxon signed-rank test; triangles: additional $n = 6$ controls without TTX).

(C) Representative dual GECI experiment. Left: QD-coated pipette adjacent to a jRCaMP1a-expressing axon (traced in cyan) approaching a GCaMP6f-expressing astrocyte. Center: Time-aligned axonal and astrocytic Ca^{2+} responses to minimal axonal stimuli, extracted in the VOIs at left (blue, axon, $11.3\ \mu\text{m}^3$; orange, astrocyte, $2.5\ \mu\text{m}^3$). Raw axonal jRCaMP1a response (cyan) overlaid with filtered trace (5 points, black). Astrocyte response is slightly delayed. TTX abolishes both axonal and astrocytic Ca^{2+} responses. Right: Close-up showing timings of axonal and astrocytic responses to the middle three stimuli. Arrows denote onset of stimuli.



Most previous studies selected the soma as the “reporter ROI” (region of interest) of the astrocytic Ca^{2+} activity, without knowing the exact nature and relative frequency of the phenomena involving this region. Via 3D imaging, we captured somatic Ca^{2+} events in their entirety and defined their relative frequency. Such events are very heterogeneous and cannot be considered a single family, as often done until now. Some of them are rather local, generated within or around the soma, and occupy only part of its volume; others are larger and occupy the whole soma together with variable proportions of the astrocytic arborization; global events are even larger. These latter seem actually to be composite events originating at multiple independent foci, which variably contribute to their overall spatiotemporal expansion (Fig. 4F and fig. S6). Even after regrouping all these heterogeneous events, total somatic activity remains very infrequent relative to activity in other compartments, counting for <3% of the total core activity recorded in vivo and 5% of the activity ex vivo. These figures may actually overestimate the somatic contribution, because in high-speed recordings we captured additional fast activity in processes and endfeet. Therefore, somatic Ca^{2+} measures do not correctly represent the astrocyte biology and are likely to lead to misinterpretation when attempting to address interactions of astrocytes with synapses and blood vessels, which may largely occur on a local basis and via fast events. This aspect needs to be highlighted because, even recently, influential studies have interpreted major issues in astrocyte biology, such as the question of the existence of gliotransmission, only on the basis of somatic Ca^{2+} measures (23).

Ca^{2+} activity in endfeet was also preponderantly local, detached from the rest of the astrocyte (including from endfoot process activity), and confined to individual endfoot domains, even to their fractions. Two or more endfeet, monitored simultaneously in different focal planes, were most often active independently, even when enwrapping contiguous segments of the same blood vessel. From time to time they underwent local coordination that also involved the respective processes, possibly in response to a local vascular input (41) or to local synaptic activity. These observations are in line with recent data showing that neuronal activity induces fast Ca^{2+} signals in endfeet but not in the soma of astrocytes. These fast endfoot signals precede the vascular response and could be involved in neurovascular coupling (20, 21). We also observed a more general level of coordination in vivo, when global Ca^{2+} events coordinated the whole astrocyte. Such events have been associated to the slow component of the blood oxygen level-dependent functional magnetic resonance imaging (BOLD fMRI) signal and would mediate a persistent vascular response to elevated neuronal activity (42).

Issues concerning the “responsivity” of astrocytes to neuronal activity—that is, whether astrocytes sense only high levels of neuronal activity (26) or also low levels (14, 15), and whether their basal Ca^{2+} activity is in part driven by neuronal activity

(11–14) or is all intrinsically generated by the astrocytes (26, 40, 43)—are currently a subject of debate. By scanning whole-astrocyte volumes during axonal stimulations, we identified small local Ca^{2+} elevations time-correlated to minimal axonal activity, often spatially contiguous to the 3D trajectory of the visible active axons. Such astrocyte Ca^{2+} spots were TTX-sensitive and already detectable in response to a single action potential pulse, strongly supporting the view that astrocytes sense even the lowest levels of neuronal activity. In addition, 3D imaging also permitted the identification of a TTX-sensitive component of the basal Ca^{2+} activity in the processes of astrocytes in hippocampal slices, which was distributed unevenly among different processes. This heterogeneity offers a reason why some previous 2D studies, which necessarily focused on individual, randomly selected processes, may have missed or underestimated this component (see supplementary text).

Our study shows that 3D Ca^{2+} imaging of entire astrocytes is possible and generates more complete and accurate information than any other approach previously used to study astrocyte Ca^{2+} dynamics. The present data provide plausible answers to several debated issues in astrocyte biology and new strategies to solve pending ones. They also highlight future challenges. For example, a large part of the astrocytic Ca^{2+} activity, including fast components of global events and focal responses to neuronal firing, is located in the gliaplil (i.e., outside the optically resolvable astrocytic structure). This calls for inclusion of detailed gliaplil studies in future investigations. However, correct reporting of gliaplil Ca^{2+} activity is beyond current technology. Only advanced superresolution techniques will allow resolution of the fine gliaplil structures, a step necessary to link signals to loci and investigate the underlying biology. New Ca^{2+} indicators capable of reaching adequate concentration in the low-volume structures without causing excessive Ca^{2+} buffering will also be required. Additional technical challenges come from the nature of the astrocyte Ca^{2+} signals, which are mostly fast, local, and scattered throughout the astrocytic territory. Only ultrafast scanning of entire astrocytes will permit proper capture of the whole gamut of signals. Here, too, current technology is limited, imposing a compromise between scanned volume, speed, and laser power deposited to the cell. Despite these challenges, the 3D nature of astrocytes and of their local interactions with synapses and blood vessels makes 3D imaging the state-of-the-art approach for future Ca^{2+} studies addressing the role of astrocytes in brain function.

Methods summary

We recorded Ca^{2+} signals from the entire 3D structure of an astrocyte with a fast-scanning two-photon microscope equipped with AOD or resonant scanner and piezoelectric objective z -actuator (routine rate, 60 focal planes/s; 2 Hz). In some experiments, we recorded from 3D subdomains (a process or an endfoot) at a faster rate (10 Hz). We used a dual-indicator approach to capture both morphology (SR101, red) and Ca^{2+} (GCaMP6f,

green) signals of astrocytes in vivo, in the somatosensory cortex of adult awake mice, and ex vivo, in acute hippocampal and cortical slices. In some experiments we collected astrocytic (GCaMP6f, green) and axonal (jRCaMP1a or tdTomato, red) signals simultaneously. To obtain conditional astrocyte-selective GCaMP6f expression, we crossed Rosa26-lsl-GCaMP6f mice with GFAP-CreERT2 mice. We analyzed the large data sets generated from our 3D imaging experiments with custom-written programs and two different analytical strategies. With the first one, we extracted Ca^{2+} events within the optically resolved astrocyte core and defined their properties. The segmented core was subdivided into macroregions (soma, processes, endfeet), and these were further split into subregions. Signals, detected subregion by subregion, were reconstructed as events by grouping adjacent simultaneously active subregions. With the second strategy, we extended the study of Ca^{2+} dynamics to the astrocytic regions with structures below optical resolution (the gliaplil). Analysis in this case was conducted structure-free, voxel by voxel. With the same approach, we analyzed astrocytic responses to minimal axonal stimulations in slices and astrocyte-wide Ca^{2+} elevations in awake mice. We used cross-correlation analysis to identify the small astrocytic regions responding to axonal stimulation or the early-responding regions during astrocyte-wide events. For studying 3D astrocyte morphology and its relations with blood vessels, we used GFAP-EGFP mice.

REFERENCES AND NOTES

1. K. E. Poskanzer, R. Yuste, Astrocytes regulate cortical state switching in vivo. *Proc. Natl. Acad. Sci. U.S.A.* **113**, E2675–E2684 (2016). doi: [10.1073/pnas.1520759113](https://doi.org/10.1073/pnas.1520759113); pmid: [27122314](https://pubmed.ncbi.nlm.nih.gov/27122314/)
2. A. Voltterra, N. Liaudet, I. Savtchouk, Astrocyte Ca^{2+} signalling: An unexpected complexity. *Nat. Rev. Neurosci.* **15**, 327–335 (2014). doi: [10.1038/nrn3725](https://doi.org/10.1038/nrn3725); pmid: [24739787](https://pubmed.ncbi.nlm.nih.gov/24739787/)
3. A. Araque et al., Gliotransmitters travel in time and space. *Neuron* **81**, 728–739 (2014). doi: [10.1016/j.neuron.2014.02.007](https://doi.org/10.1016/j.neuron.2014.02.007); pmid: [24559669](https://pubmed.ncbi.nlm.nih.gov/24559669/)
4. G. Perea, M. Navarrete, A. Araque, Tripartite synapses: Astrocytes process and control synaptic information. *Trends Neurosci.* **32**, 421–431 (2009). doi: [10.1016/j.tins.2009.05.001](https://doi.org/10.1016/j.tins.2009.05.001); pmid: [19615761](https://pubmed.ncbi.nlm.nih.gov/19615761/)
5. N. Bazargani, D. Attwell, Astrocyte calcium signaling: The third wave. *Nat. Neurosci.* **19**, 182–189 (2016). doi: [10.1038/nn.4201](https://doi.org/10.1038/nn.4201); pmid: [26814587](https://pubmed.ncbi.nlm.nih.gov/26814587/)
6. B. A. MacVicar, E. A. Newman, Astrocyte regulation of blood flow in the brain. *Cold Spring Harb. Perspect. Biol.* **7**, a020388 (2015). doi: [10.1101/cshperspect.a020388](https://doi.org/10.1101/cshperspect.a020388); pmid: [25818565](https://pubmed.ncbi.nlm.nih.gov/25818565/)
7. J. Schummers, H. Yu, M. Sur, Tuned responses of astrocytes and their influence on hemodynamic signals in the visual cortex. *Science* **320**, 1638–1643 (2008). doi: [10.1126/science.1156120](https://doi.org/10.1126/science.1156120); pmid: [18566287](https://pubmed.ncbi.nlm.nih.gov/18566287/)
8. A. Nimmerjahn, E. A. Mukamel, M. J. Schnitzer, Motor behavior activates Bergmann glial networks. *Neuron* **62**, 400–412 (2009). doi: [10.1016/j.neuron.2009.03.019](https://doi.org/10.1016/j.neuron.2009.03.019); pmid: [19447095](https://pubmed.ncbi.nlm.nih.gov/19447095/)
9. K. Kanemaru et al., In vivo visualization of subtle, transient, and local activity of astrocytes using an ultrasensitive Ca^{2+} indicator. *Cell Rep.* **8**, 311–318 (2014). doi: [10.1016/j.celrep.2014.05.056](https://doi.org/10.1016/j.celrep.2014.05.056); pmid: [24981861](https://pubmed.ncbi.nlm.nih.gov/24981861/)
10. X. Wang et al., Astrocytic Ca^{2+} signaling evoked by sensory stimulation in vivo. *Nat. Neurosci.* **9**, 816–823 (2006). doi: [10.1038/nn1703](https://doi.org/10.1038/nn1703); pmid: [16699507](https://pubmed.ncbi.nlm.nih.gov/16699507/)
11. M. Navarrete et al., Astrocytes mediate in vivo cholinergic-induced synaptic plasticity. *PLoS Biol.* **10**, e1001259 (2012). doi: [10.1371/journal.pbio.1001259](https://doi.org/10.1371/journal.pbio.1001259); pmid: [22347811](https://pubmed.ncbi.nlm.nih.gov/22347811/)
12. C. Henneberger, T. Papouin, S. H. Oliet, D. A. Rusakov, Long-term potentiation depends on release of D-serine from astrocytes. *Nature* **463**, 232–236 (2010). doi: [10.1038/nature08673](https://doi.org/10.1038/nature08673); pmid: [20075918](https://pubmed.ncbi.nlm.nih.gov/20075918/)

13. R. Min, T. Nevian, Astrocyte signaling controls spike timing-dependent depression at neocortical synapses. *Nat. Neurosci.* **15**, 746–753 (2012). doi: [10.1038/nn.3075](https://doi.org/10.1038/nn.3075); pmid: [22446881](https://pubmed.ncbi.nlm.nih.gov/22446881/)
14. M. A. Di Castro *et al.*, Local Ca²⁺ detection and modulation of synaptic release by astrocytes. *Nat. Neurosci.* **14**, 1276–1284 (2011). doi: [10.1038/nn.2929](https://doi.org/10.1038/nn.2929); pmid: [21909085](https://pubmed.ncbi.nlm.nih.gov/21909085/)
15. A. Panatier *et al.*, Astrocytes are endogenous regulators of basal transmission at central synapses. *Cell* **146**, 785–798 (2011). doi: [10.1016/j.cell.2011.07.022](https://doi.org/10.1016/j.cell.2011.07.022); pmid: [21855979](https://pubmed.ncbi.nlm.nih.gov/21855979/)
16. G. R. Gordon, H. B. Choi, R. L. Rungta, G. C. Ellis-Davies, B. A. MacVicar, Brain metabolism dictates the polarity of astrocyte control over arterioles. *Nature* **456**, 745–749 (2008). doi: [10.1038/nature07525](https://doi.org/10.1038/nature07525); pmid: [18971930](https://pubmed.ncbi.nlm.nih.gov/18971930/)
17. I. R. Winship, N. Plaa, T. H. Murphy, Rapid astrocyte calcium signals correlate with neuronal activity and onset of the hemodynamic response in vivo. *J. Neurosci.* **27**, 6268–6272 (2007). doi: [10.1523/JNEUROSCI.4801-06.2007](https://doi.org/10.1523/JNEUROSCI.4801-06.2007); pmid: [17554000](https://pubmed.ncbi.nlm.nih.gov/17554000/)
18. H. L. Xu *et al.*, Astrocytes are a key conduit for upstream signaling of vasodilation during cerebral cortical neuronal activation in vivo. *Am. J. Physiol. Heart Circ. Physiol.* **294**, H622–H632 (2008). doi: [10.1152/ajpheart.00530.2007](https://doi.org/10.1152/ajpheart.00530.2007); pmid: [18055520](https://pubmed.ncbi.nlm.nih.gov/18055520/)
19. M. R. Metea, E. A. Newman, Glial cells dilate and constrict blood vessels: A mechanism of neurovascular coupling. *J. Neurosci.* **26**, 2862–2870 (2006). doi: [10.1523/JNEUROSCI.4048-05.2006](https://doi.org/10.1523/JNEUROSCI.4048-05.2006); pmid: [16540563](https://pubmed.ncbi.nlm.nih.gov/16540563/)
20. B. L. Lind, A. R. Brazhe, S. B. Jessen, F. C. Tan, M. J. Lauritzen, Rapid stimulus-evoked astrocyte Ca²⁺ elevations and hemodynamic responses in mouse somatosensory cortex in vivo. *Proc. Natl. Acad. Sci. U.S.A.* **110**, E4678–E4687 (2013). doi: [10.1073/pnas.1310065110](https://doi.org/10.1073/pnas.1310065110); pmid: [24218625](https://pubmed.ncbi.nlm.nih.gov/24218625/)
21. Y. Otsu *et al.*, Calcium dynamics in astrocyte processes during neurovascular coupling. *Nat. Neurosci.* **18**, 210–218 (2015). doi: [10.1038/nn.3906](https://doi.org/10.1038/nn.3906); pmid: [25531572](https://pubmed.ncbi.nlm.nih.gov/25531572/)
22. C. Agulhon, T. A. Fiacco, K. D. McCarthy, Hippocampal short- and long-term plasticity are not modulated by astrocyte Ca²⁺ signaling. *Science* **327**, 1250–1254 (2010). doi: [10.1126/science.1184821](https://doi.org/10.1126/science.1184821); pmid: [20203048](https://pubmed.ncbi.nlm.nih.gov/20203048/)
23. W. Sun *et al.*, Glutamate-dependent neuroglial calcium signaling differs between young and adult brain. *Science* **339**, 197–200 (2013). doi: [10.1126/science.1226740](https://doi.org/10.1126/science.1226740); pmid: [23307741](https://pubmed.ncbi.nlm.nih.gov/23307741/)
24. K. Nizar *et al.*, In vivo stimulus-induced vasodilation occurs without IP3 receptor activation and may precede astrocytic calcium increase. *J. Neurosci.* **33**, 8411–8422 (2013). doi: [10.1523/JNEUROSCI.3285-12.2013](https://doi.org/10.1523/JNEUROSCI.3285-12.2013); pmid: [23658179](https://pubmed.ncbi.nlm.nih.gov/23658179/)
25. D. E. Bonder, K. D. McCarthy, Astrocytic Gq-GPCR-linked IP3R-dependent Ca²⁺ signaling does not mediate neurovascular coupling in mouse visual cortex in vivo. *J. Neurosci.* **34**, 13139–13150 (2014). doi: [10.1523/JNEUROSCI.2591-14.2014](https://doi.org/10.1523/JNEUROSCI.2591-14.2014); pmid: [25253859](https://pubmed.ncbi.nlm.nih.gov/25253859/)
26. M. D. Haustein *et al.*, Conditions and constraints for astrocyte calcium signaling in the hippocampal mossy fiber pathway. *Neuron* **82**, 413–429 (2014). doi: [10.1016/j.neuron.2014.02.041](https://doi.org/10.1016/j.neuron.2014.02.041); pmid: [24742463](https://pubmed.ncbi.nlm.nih.gov/24742463/)
27. W. Göbel, B. M. Kampa, F. Helmchen, Imaging cellular network dynamics in three dimensions using fast 3D laser scanning. *Nat. Methods* **4**, 73–79 (2007). doi: [10.1038/nmeth989](https://doi.org/10.1038/nmeth989); pmid: [17143280](https://pubmed.ncbi.nlm.nih.gov/17143280/)
28. T. W. Chen *et al.*, Ultrasensitive fluorescent proteins for imaging neuronal activity. *Nature* **499**, 295–300 (2013). doi: [10.1038/nature12354](https://doi.org/10.1038/nature12354); pmid: [23868258](https://pubmed.ncbi.nlm.nih.gov/23868258/)
29. H. Dana *et al.*, Sensitive red protein calcium indicators for imaging neural activity. *eLife* **5**, e12727 (2016). doi: [10.7554/eLife.12727](https://doi.org/10.7554/eLife.12727); pmid: [27011354](https://pubmed.ncbi.nlm.nih.gov/27011354/)
30. See supplementary materials.
31. R. Srinivasan *et al.*, Ca²⁺ signaling in astrocytes from *Ip3r2*^{-/-} mice in brain slices and during startle responses in vivo. *Nat. Neurosci.* **18**, 708–717 (2015). doi: [10.1038/nn.4001](https://doi.org/10.1038/nn.4001); pmid: [25894291](https://pubmed.ncbi.nlm.nih.gov/25894291/)
32. K. J. Sekiguchi *et al.*, Imaging large-scale cellular activity in spinal cord of freely behaving mice. *Nat. Commun.* **7**, 11450 (2016). doi: [10.1038/ncomms11450](https://doi.org/10.1038/ncomms11450); pmid: [27121084](https://pubmed.ncbi.nlm.nih.gov/27121084/)
33. P. O. Polack, J. Friedman, P. Golshani, Cellular mechanisms of brain state-dependent gain modulation in visual cortex. *Nat. Neurosci.* **16**, 1331–1339 (2013). doi: [10.1038/nn.3464](https://doi.org/10.1038/nn.3464); pmid: [23872595](https://pubmed.ncbi.nlm.nih.gov/23872595/)
34. M. Avoli *et al.*, Synchronous GABA-mediated potentials and epileptiform discharges in the rat limbic system in vitro. *J. Neurosci.* **16**, 3912–3924 (1996). pmid: [8656285](https://pubmed.ncbi.nlm.nih.gov/8656285/)
35. M. P. Witter, The perforant path: Projections from the entorhinal cortex to the dentate gyrus. *Prog. Brain Res.* **163**, 43–61 (2007). doi: [10.1016/S0079-6123\(07\)63003-9](https://doi.org/10.1016/S0079-6123(07)63003-9); pmid: [17765711](https://pubmed.ncbi.nlm.nih.gov/17765711/)
36. N. V. Povyshva *et al.*, Properties of excitatory synaptic responses in fast-spiking interneurons and pyramidal cells from monkey and rat prefrontal cortex. *Cereb. Cortex* **16**, 541–552 (2006). doi: [10.1093/cercor/bhj002](https://doi.org/10.1093/cercor/bhj002); pmid: [16033926](https://pubmed.ncbi.nlm.nih.gov/16033926/)
37. M. Paukert *et al.*, Norepinephrine controls astroglial responsiveness to local circuit activity. *Neuron* **82**, 1263–1270 (2014). doi: [10.1016/j.neuron.2014.04.038](https://doi.org/10.1016/j.neuron.2014.04.038); pmid: [24945771](https://pubmed.ncbi.nlm.nih.gov/24945771/)
38. K. Zheng *et al.*, Time-resolved imaging reveals heterogeneous landscapes of nanomolar Ca²⁺ in neurons and astroglia. *Neuron* **88**, 277–288 (2015). doi: [10.1016/j.neuron.2015.09.043](https://doi.org/10.1016/j.neuron.2015.09.043); pmid: [26494277](https://pubmed.ncbi.nlm.nih.gov/26494277/)
39. J. G. Jackson, M. B. Robinson, Reciprocal regulation of mitochondrial dynamics and calcium signaling in astrocyte processes. *J. Neurosci.* **35**, 15199–15213 (2015). doi: [10.1523/JNEUROSCI.2049-15.2015](https://doi.org/10.1523/JNEUROSCI.2049-15.2015); pmid: [26558789](https://pubmed.ncbi.nlm.nih.gov/26558789/)
40. A. Agarwal *et al.*, Transient opening of the mitochondrial permeability transition pore induces microdomain calcium transients in astrocyte processes. *Neuron* **93**, 587–605.e7 (2017). doi: [10.1523/JNEUROSCI.2049-15.2015](https://doi.org/10.1523/JNEUROSCI.2049-15.2015); pmid: [26558789](https://pubmed.ncbi.nlm.nih.gov/26558789/)
41. K. J. Kim *et al.*, Astrocyte contributions to flow/pressure-evoked parenchymal arteriole vasoconstriction. *J. Neurosci.* **35**, 8245–8257 (2015). doi: [10.1523/JNEUROSCI.4486-14.2015](https://doi.org/10.1523/JNEUROSCI.4486-14.2015); pmid: [26019339](https://pubmed.ncbi.nlm.nih.gov/26019339/)
42. K. Schulz *et al.*, Simultaneous BOLD fMRI and fiber-optic calcium recording in rat neocortex. *Nat. Methods* **9**, 597–602 (2012). doi: [10.1038/nmeth.2013](https://doi.org/10.1038/nmeth.2013); pmid: [22561989](https://pubmed.ncbi.nlm.nih.gov/22561989/)
43. W. J. Nett, S. H. Oloff, K. D. McCarthy, Hippocampal astrocytes in situ exhibit calcium oscillations that occur independent of neuronal activity. *J. Neurophysiol.* **87**, 528–537 (2002). pmid: [11784768](https://pubmed.ncbi.nlm.nih.gov/11784768/)

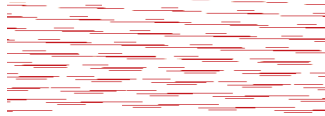
ACKNOWLEDGMENTS

We thank some of our former and present students in the lab who contributed to various extents to specific parts of the present study: C. Dürst, C. Navarro, A.-A. Dumont, and T. Mergiya. We thank H. Stubbe and E. Hugonnet for maintaining our mouse colony. We also thank N. Toni for introducing our group to the use and modalities of viral injections in the entorhinal cortex. Transgenic Rosa26-*Isl1*-GCaMP6f mice [Gt (ROSA)26Sortm95.1 (CAGGCaMP6f)Hze] are available from Charles River under a material transfer agreement with the Jackson Laboratory; viral constructs AAV1-Syn-NES-jRCaMP1 and AAV5.CamKII:Cre virus are available from Penn/Vector Core under a material transfer agreement; the same for pQC TdTomato IX plasmid from Addgene. jRCaMP1a construct was supplied by L. L. Looger (whom we thank for helpful discussions and generosity), V. Jayaraman, D. S. Kim, and K. Svoboda from the GENIE Project, Janelia Research Campus, Howard Hughes Medical Institute. GFAP-CreERT2 mice were generously provided by F. Kirchhoff. Supported by ERC advanced grant 340368 “Astromnesia” and Swiss National Science Foundation grants 31003A-140999 and 31003A-173124/1 (A.V.) and by the National Centers of Competence in Research (NCCR) “Transcure” and “Synapsy,” of which A.V. is one of the principal investigators. Data are stored in a database on the authors’ institution server and are available from the corresponding author upon reasonable request. Author contributions: E.B. performed all the Ca²⁺ imaging experiments in astrocytes in brain slices and part of the experiments in awake mice, performed the related analyses, and participated in analysis development and writing of the manuscript; I.S. developed and performed the experiments on axon-astrocyte interactions and related data analysis, supervised some of the experiments in brain slices, participated in experiments in vivo in awake mice, developed analytical tools, participated in the development of the main analysis methods, and contributed to the writing of the paper; N.L. developed the main original analytical methods used in the study, created user-friendly software for the other authors, interacted with companies and other authors to define the appropriate microscopy tools and conditions for 3D dynamic imaging, performed data analysis, and participated in writing of the manuscript; D.B. developed and performed Ca²⁺ imaging in awake mice, performed immunohistochemistry and data analysis, and participated in the writing of the manuscript; G.C. performed all the viral injections and two-photon acquisitions for morphometric analyses and participated in the in vivo experiments in awake mice; and A.V. conceived and supervised the project and wrote the manuscript together with the other authors.

SUPPLEMENTARY MATERIALS

www.sciencemag.org/content/356/6339/eaai8185/suppl/DC1
Materials and Methods
Supplementary Text
Figs. S1 to S11
Table S1
Movies S1 to S4
References (44–61)

16 August 2016; accepted 12 April 2017
[10.1126/science.aai8185](https://doi.org/10.1126/science.aai8185)



Three-dimensional Ca²⁺ imaging advances understanding of astrocyte biology

Erika Bindocci, Iaroslav Savtchouk, Nicolas Liaudet, Denise Becker, Giovanni Carriero and Andrea Volterra (May 18, 2017) *Science* **356** (6339), . [doi: 10.1126/science.aai8185]

Editor's Summary

Glial calcium dynamics in space and time

Astrocytes use calcium signals to process information received from neighboring brain cells and thus generate modulatory responses at the local or network level. Previous studies have relied on calcium imaging in line scans or in a single focal plane mostly focusing on the cell bodies of astrocytes. Bindocci *et al.* used more powerful scanners that can rapidly scan many focal planes. They combined this technique with advanced genetic tools for monitoring calcium gradients with high sensitivity, which allowed three-dimensional calcium imaging of a whole astrocyte. Most of the basal calcium activity occurred in the astrocyte processes, some in the endfeet, and only a small fraction actually in the cell bodies of astrocytes.

Science, this issue p. eaai8185

This copy is for your personal, non-commercial use only.

Article Tools Visit the online version of this article to access the personalization and article tools:
<http://science.sciencemag.org/content/356/6339/eaai8185>

Permissions Obtain information about reproducing this article:
<http://www.sciencemag.org/about/permissions.dtl>

Science (print ISSN 0036-8075; online ISSN 1095-9203) is published weekly, except the last week in December, by the American Association for the Advancement of Science, 1200 New York Avenue NW, Washington, DC 20005. Copyright 2016 by the American Association for the Advancement of Science; all rights reserved. The title *Science* is a registered trademark of AAAS.